Journal of Applied Polymer Science

Effects of the Carboxyl-Ended Hyperbranched Polyester/Platinum Complex Molecular Weight on Hydrosilylation Activity and Self-Assembled Morphology

Zhicai Xu,[1] Daohong Zhang,[1] Junna Li,[1] Sufang Chen,[2] Tingcheng Li,[1] Junheng Zhang,[1] Aiqing Zhang,[1] Shenghui Chen[3]

[1]Key Laboratory of Catalysis and Materials Science of the State Ethnic Affairs Commission & Ministry of Education, South-Central University for Nationalities, Wuhan, Hubei Province 430074, China

[2]Key Laboratory for Green Chemical Process of Ministry of Education, Wuhan Institute of Technology, Wuhan, Hubei 430073, China

[3]College of Chemistry and Materials Science, South-Central University for Nationalities, Wuhan, Hubei Province, 430074, China

Correspondence to: D. Zhang (E-mail: zhangdh27@163.com) and S. Chen (E-mail: chenshenghui03@yahoo.com.cn)

ABSTRACT: Research on platinum catalysts with high activity and long life for hydrosilylation has attracted a great deal of interest because of the increasing price of platinum metal. In this study, we examined the effect of the molecular weight of carboxyl-ended hyperbranched polyester/platinum complexes (HTD-*n*–Pt's, where $n = 1$, 2, 3, or 4) on hydrosilylation activity and self-assembled morphology. Relevant parameters tuning the morphology of self-assemblies, such as the temperature, time, concentration, and relative humidity, were examined. All of the HTD-*n*–Pt's with various molecular weights had much higher hydrosilylation activities than did the conventional homogeneous Speier's catalyst, and the HTD-*n*–Pt could be self-assembled into ordered two-dimensional treelike structures with a fractal dimension ranging from 1.48 to 1.83; this indicated perfect fractal properties. With the increase of the HTD-*n*–Pt molecular weight, the size of the self-assembled treelike structures and the catalytic activity increased first and then decreased. The self-assembly mechanism was speculated and analyzed by dynamic light scattering, X-ray photoelectron spectroscopy, X-ray diffraction, scanning electron microscopy, and Fourier transform infrared spectroscopy; these suggested good agreement with the diffusion-limited aggregation theory of particles. © 2014 Wiley Periodicals, Inc. J. Appl. Polym. Sci. **2015**, *132*, 41416.

KEYWORDS: morphology; properties and characterization; self-assembly

Received 29 May 2014; accepted 18 August 2014

DOI: 10.1002/app.41416

INTRODUCTION

The hydrosilylation of olefins is a crucial catalytic reaction for producing industrially important organosilicon compounds, such as organofunctional silanes and silicones,[1] and for cross-linking silicone polymers to elastomers and silicone-based release coatings. As the industrially most important Pt-based catalysts for this reaction, a homogeneous platinum catalyst[2] was very active but difficult to recycle. However, recyclable heterogeneous platinum catalysts are usually less active. Research on the development of highly active and reusable catalysts for hydrosilylation has been of great interest because of the scarcity and high price of platinum. The challenge generally lies in how to improve the dispersion of active platinum on various supports.[1]

Hyperbranched polymers (HBPs) with different topologies and molecular sizes are randomly branched macromolecules, prepared through a one-step polymerization process.[3,4] HBPs have been used broadly as supports for various fields, including catalysis,[5] drug carriers,[6] and biomaterials,[7–12] containing a large number of terminal functional groups. HBPs may show amphiphilic and nonamphiphilic properties according to the hydrophilicity difference of their core segments and peripheral groups. The morphology of stable self-assemblies[13] is easily controlled by the tuning of the ratio of hydrophilic and hydrophobic segments in amphiphilic HBPs. The self-assembled morphologies, including spherical micelles, cylindrical micelles, discontinuous structures, fibers, tubes, lamellae, and vesicles, are primarily determined by a packing parameter,[13] $p = v/a_0 l_c$, where v is the volume of the hydrophobic segment, a_0 is the contact area of the head group, and l_c is the length of the hydrophobic segment. Therefore, the design and synthesis of amphiphilic HBPs with hydrophobic segment of proper length of are pivotal to the self-assembly of amphiphilic HBPs.

© 2014 Wiley Periodicals, Inc.

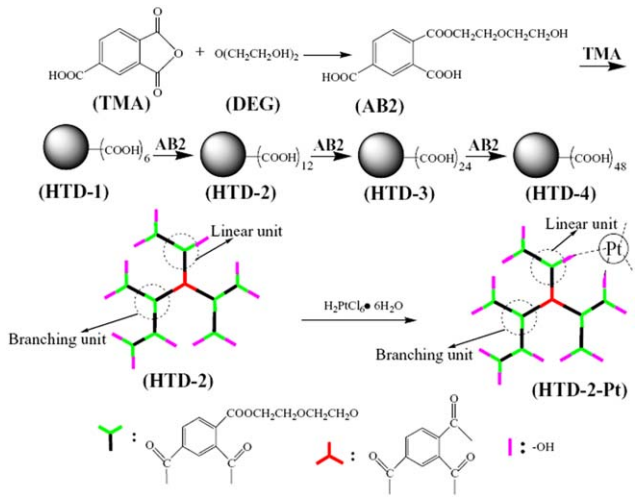

Figure 1. Synthesis schemes for HTD-*n* and HTD-2–Pt. AB2 = chemical structure. [Color figure can be viewed in the online issue, which is available at wileyonlinelibrary.com.]

Amphiphilic HBPs[6,11,14] have demonstrated great success and have been well developed in self-assembly for their applications[11,12,15–17] as biomaterials and drug-delivery and reaction vessels.[11] However, complex and tedious synthetic processes, such as grafting modification or reversible addition–fragmentation chain-transfer polymerization copolymerization,[11,12] have limited their practical applications. Nonamphiphilic HBPs can be obtained from facile one-pot or pseudo-one-step methods, and they contain various functional terminals, such as carboxyl-, hydroxyl-, vinyl-, amino-, or amido-ended groups; these may provide unique properties in the encapsulation of small molecules or inorganic nanoparticles.[4,18] Although directly self-assembling nonamphiphilic HBPs into an ordered structure is a challenge, we first obtained ordered microrods and treelike aggregates by the self-assembly of carboxyl-ended hyperbranched polyesters (HTD-*n*'s, where $n = 1$, 2, 3, or 4) via the coordination induction of platinum,[5,19] copper,[20] and ferric[21] ions. Platinum coordination played a key role in driving the microphase separation between the intermolecular and peripheral chains of the carboxyl-ended hyperbranched polyester/platinum complexes (HTD-*n*–Pt's, where $n = 1$, 2, 3, or 4; e.g., HTD-3–Pt and HTD-2–Pt). Because the solubility parameter of a pyridine/ethyl acetate solution [19.80 $(J/cm^3)^{0.5}$] is an approach to that of the core segments [19.47 $(J/cm^3)^{0.5}$], the pyridine/ethyl acetate can dissolve the core segments but it is not the peripheral groups for the formation of water/oil micelles. On the contrary, if a selected solvent should dissolve the peripheral groups rather than core segments for the formation of oil/water micelles, it is a challenge to control the self-assembled morphology. Both HTD-3–Pt and HTD-2–Pt[19] could be self-assembled into low-dimension, micrometer-sized lamellar films in tetrahydrofuran (THF) and microrods[5] on the surface of the glass substrate, but amido-ended group HBPs[22,23] with stronger hydrogen-bonding interaction could be self-assembled into two-dimensional (2D) treelike structures. Moreover, both HTD-3–Pt and HTD-2–Pt showed higher catalytic properties for hydrosilylation than traditional catalysts. The influence of the molecular weight and the properties (e.g., hydrophilicity) of a solvent on the morphology of the resulting self-assemblies still remains undiscovered as does that on the catalytic activity of the complex (HTD-*n*–Pt).

In this study, we synthesized HTD-*n*–Pt's with various molecular weights and examined the effects of the HTD-*n*–Pt molecular weight on the catalytic activity of hydrosilylation and their surface self-assembled 2D treelike structure. The self-assembly mechanism was investigated with dynamic light scattering (DLS), scanning electron microscopy, X-ray diffraction (XRD), X-ray photoelectron spectroscopy (XPS), and Fourier transform infrared (FTIR) spectroscopy. The novel treelike self-assemblies may hopefully be used as multifunctional drug carriers in release system because of the function of the platinum ions[24] for the improvement of bioactive materials and as bioactive materials themselves[9] because of their fractal properties.[25]

EXPERIMENTAL

Materials and Instruments

Trimellitic anhydride, xylene, diethylene glycol, tetrabutyl titanate, dimethylformamide (DMF), chloroplatinic acid, THF, 1,1,3,3-tetramethyldisiloxane (TMDS), styrene (St), and NH_4HCO_3 were analytical grade and were purchased from Sinopharm Chemical Reagent Corp. All of the reagents were used without further purification unless noted otherwise.

FTIR measurements were performed on a Bruker Vector 33 spectrometer with a sealed cell (KBr, 0.5 mm). ^{1}H-NMR measurements was conducted on an Avance Ⅲ-400 (Bruker) NMR spectrometer with hexadeuterated dimethyl sulfoxide as the solvent. A low-voltage scanning electron microscope (XL-30FEG, Philips) and a transmission/reflection polarizing optical microscope (TRPOM; XPV-203E, China) equipped with a thermal platform were used to examine the morphology of the self-assemblies. The XRD patterns were obtained with a Bruker-D8 diffractometer with monochromatized Cu Kα radiation ($\lambda = 1.54$ Å). The surface compositions of the samples were determined with a Vacuum Generator Mutilab 2000 XPS spectrometer with the C1s (284.6 eV) peak of the contamination carbon as the internal standard. DLS measurements of samples with a concentration of 1.0 mg/mL were performed on a ZetaSizer Nano ZS90 (Malvern Instrument, Worcs, United Kingdom) equipped with a 4-mW He–Ne Laser at about 25.0°C and at a scattering angle of 90°. The apparent *z*-average hydrodynamic diameter (D_h) was calculated by the dispersion technology software provided by Malvern.

Preparation of the HTD-*n*–Pt

The synthesis scheme of HTD-2–Pt is shown in Figure 1. First, the HTD-*n*'s were synthesized according to our previous articles,[26,27] as shown in Figure 1. Their molecular weights and distributions are shown in Table I. The characteristic groups of the HTD-*n*'s were identified.

FTIR spectroscopy (KCl, cm^{-1}): 3300–3500 (s, —OH), 1730 (s, —COO—), 1660 (s, —COOH). ^{1}H-NMR (hexadeuterated dimethyl sulfoxide, ppm, δ): 4.36–4.38 (—$COOCH_2$—), 3.67–3.74 (—CH_2OCH_2—), 7.75–8.22 (—C_6H_3).

The detailed synthetic process of HTD-2–Pt was referred to in our previous article[19] on the basis of the main materials of

Table I. Properties of HTD-*n*

	HTD-*n*			
	HTD-1	HTD-2	HTD-3	THD-4
Number of carboxyl-ended groups	6	12	24	48
M_n (Da)	2027	4260	5958	16,166
PDI = M_w/M_n	1.95	2.23	1.60	1.11
Degree of branching	0.65	0.71	0.66	0.62
Hydrophobic segment content (wt %)	74.3	80.2	82.3	83.2
Hydrophilic segment content (wt %)	25.7	19.8	17.7	16.8

M_n = number-average molecular weight; M_w = weight-average molecular weight; PDI = polydispersity index.

chloroplatinic acid (0.2 g), isopropyl alcohol (6 g), THF (3 g), HTD-2 (1 g), and NH_4HCO_3 (0.4 g). HTD-1–Pt, HTD-3–Pt, and HTD-4–Pt were also obtained through a similar process. HTD-*n*–Pt contained about 7.0 wt % platinum.

Catalytic Experiment of the HTD-*n*–Pt's

HTD-*n*–Pt (0.1 g) as a catalyst was added to a flask for hydrosilylation between St (0.06 mol, 6.24 g) and TMDS (0.025 mol, 3.36 g) at 323–328 K with mechanical stirring. The catalytic activity of the catalyst was characterized by the conversion of the Si—H bond and recorded by FTIR spectroscopy through the monitoring of the change in the $\nu_{Si—H}$ peak area at about 2121 cm^{-1} with the reaction time. Similarly, as a comparable experiment, a traditional homogeneous Speier's catalyst containing the same amount of platinum was used to catalyze the hydrosilylation.

Preparation of the Self-Assembled HTD-*n*–Pt's

In a typical experiment, HTD-2–Pt was dispersed in DMF, ultrasonication followed for 20 min. The solution was dropped on the clean surface of a glass substrate to allow for self-assembly. The self-assembled morphology was observed real in time by the TRPOM under a designated temperature and relative humidity (RH).

RESULTS AND DISCUSSION

Characterization of the HTD-*n*–Pt's

The FTIR spectra of the HTD-*n*–Pt catalysts are presented in Figure 2(a). Only the FTIR spectrum of HTD-2 is provided as an example of HTD-*n* for comparison because of their similarity of chemical structure. The absorption peaks of the ester (—COO—) and carboxyl (—COOH) groups of HTD-2 were observed at 1723 and 1650 cm^{-1}, respectively. With the reaction of $H_2PtCl_6{\cdot}6H_2O$, a new strong peak at 1610 cm^{-1} appeared and was attributed to the stretching vibrations of coordinated bonds (—COOPt),[28] and the absorption peak at 1650 cm^{-1} became weaker [Figure 2(a)]. This confirmed the coordination interactions between platinum and the carboxyl groups.

The XPS spectra of HTD-2 and HTD-*n*–Pt are shown in Figure 2(b). The peaks of the binding energy (BE) at about 285 and 532 eV were attributed to C1s and O1s electrons, respectively. The XPS spectra around the ranges of 526–536, 279–292, and 68–82 eV are shown in Figure 2(c–d). After HTD-*n* (e.g., HTD-2) reacted with chloroplatinic acid, the BE for the O1s electrons decreased from 532.1 to 531.8 eV, the C1s peak of the carboxyl group at 288.8 eV became weaker [Figure 2(c)], and the Cl2p peak at 198.8 eV disappeared. This gave further evidence for the coordination between platinum ions and the carboxyl group of HTD-*n*.[29] The peaks around 73.0 and 76.3 eV [Figure 2(d)] were attributed to $Pt_4f_{7/2}$ and $Pt_4f_{5/2}$ electrons, confirming the presence of Pt (IV) in the HTD-*n*–Pt catalysts because the BEs of the $Pt_4f_{7/2}$ and $Pt_4f_{5/2}$ electrons of Pt(0) usually appear at about 71.2 and 74.5 eV.[30]

Catalytic Properties of the HTD-*n*–Pt's

The relationship between the conversion of the Si—H bond and the reaction time was investigated and is shown in Figure 3(a) for catalysts with different molecular weights. All of the catalytic activities of these HTD-*n*–Pt catalysts were much higher than that of the Speier's catalyst containing the same platinum content. An interesting result was that the reaction catalyzed by HTD-*n*–Pt was composed of two distinct stages and explained by the following mechanism of hydrosilylation.[5,19] The solubility parameters of the core segments of HTD-1–Pt, HTD-2–Pt, HTD-3–Pt, and HTD-4–Pt were 19.36, 19.44, 19.47, and 19.48 $(J/cm^3)^{0.5}$, respectively, all of which were higher than that of St [18.90 $(J/cm^3)^{0.5}$]; this favored the HTD-*n*–Pt's as nanoparticles dispersed in the St/TMDS solution, as demonstrated by their transmission electron micrograph.[19] Hydrosilylation contains three main processes according to the modified Chalk–Harrod mechanism of hydrosilylation;[1] these include the oxidative addition between TMDS and HTD-*n*–Pt, alkene insertion, and reductive elimination. The intramolecular chains of the complex produced by alkene insertion could not dissolve completely in the St/TMDS solution; however, the peripheral segments dissolved easily because of the similarity of the solubility parameters; this resulted in the shrinkage of the intramolecular chains and the extension of the peripheral chains.[19] Therefore, more platinum active sites were exposed and were available for the catalytic reaction. Additionally, an increase in the viscosity of the system due to the coordination between the active Pt cores of the HTD-*n*–Pt's and TMDS resulted in a reduction in the reductive elimination rate. When most of the TMDS in solution was consumed, the elimination process took over; this reduced

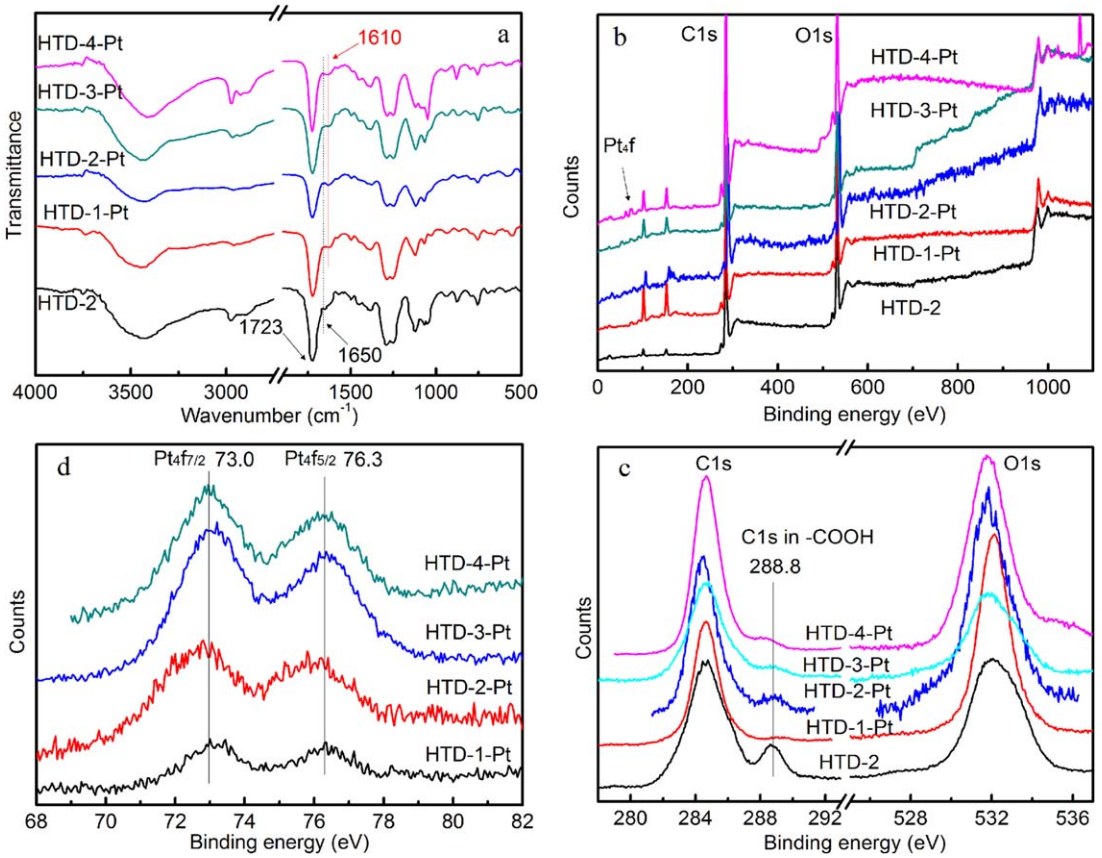

Figure 2. FTIR and XPS spectra of HTD-2 and HTD-*n*–Pt. [Color figure can be viewed in the online issue, which is available at wileyonlinelibrary.com.]

the viscosity of the system and resulted in an increase in the catalytic activity. Therefore, all of the Si—H conversion curves in Figure 3(a) showed two stages for the reaction in the presence of HTD-*n*–Pt. In comparison, the reaction rate of the homogeneous Speier's catalyst system had no such variation.

With increasing molecular weight of HTD-*n*–Pt, the catalytic activity increased first and then decreased. Both HTD-2–Pt and HTD-3–Pt catalysts with medium molecular weights had relatively higher activities than either HTD-1–Pt or HTD-4–Pt. This phenomenon may have been due to the differences in the molecular shape. The size of about $2.0 \times 0.9 \times 3.7$ nm^3 of HTD-1 was close to that of the linear polymer,[31] and the entanglement of the molecular chains might have wrapped some active Pt species during the reaction and resulted in a low activity. HTD-4, with a size of $5.9 \times 5.5 \times 10.3$ nm^3, might also have wrapped some Pt during the reaction because of its elliptic shape and high molecular weight.

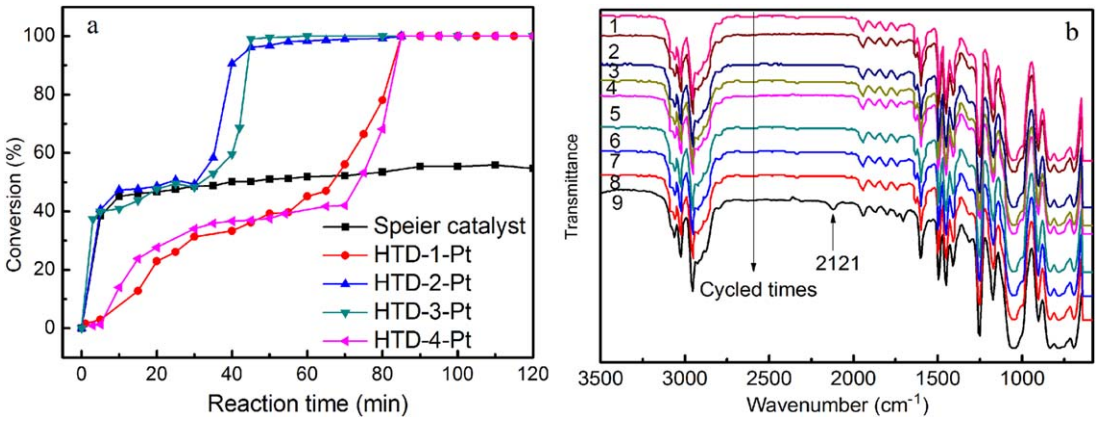

Figure 3. Effect of various catalysts for hydrosilylation on the conversion of the Si—H bond with the reaction time and cycled times. [Color figure can be viewed in the online issue, which is available at wileyonlinelibrary.com.]

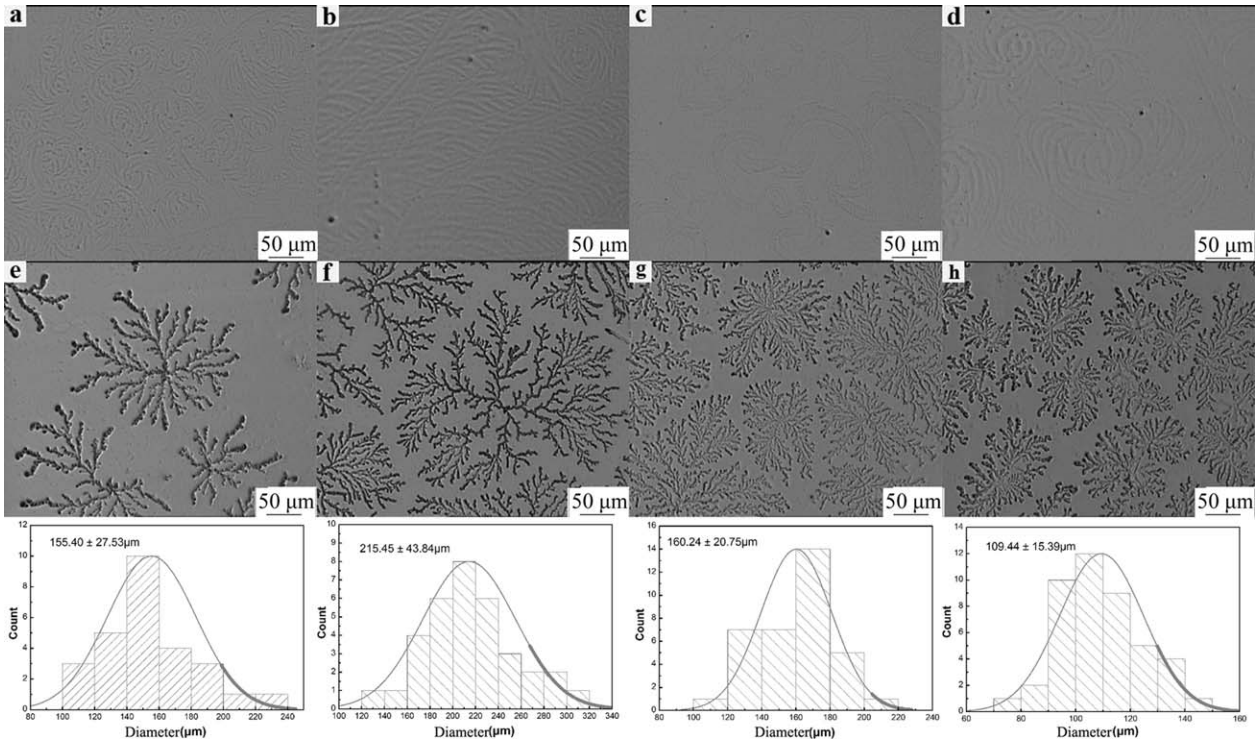

Figure 4. OM micrographs of the self-assemblies: (a) HTD-1, (b) HTD-2, (c) HTD-3,(d) HTD-4, (e) HTD-1–Pt, (f) HTD-2–Pt, (g) HTD-3–Pt, and (h) HTD-4–Pt.

The effect of the recycle time on the catalytic activity was monitored by FTIR spectroscopy and is shown in Figure 3(b). As demonstrated by the variation of the absorption peak at 2121 cm^{-1} ($\nu_{Si—H}$), the catalytic activity did not begin to diminish until the ninth run; this suggested excellent recyclability of the catalyst.

Surface Self-Assembly Morphology and Mechanism of the HTD-*n*–Pt's

Self-Assembled Morphology. The formation of thermodynamically stable self-assemblies with various morphologies is tuned by three main contributions in the free energy of the system: the stretching degree of the core-forming blocks, the interfacial tension between the micelle core and the solvent outside the core, and the repulsive interactions among the micelles.[32,33] Therefore, we examined some crucial factors, including the polymer composition, concentration, temperature, presence of additives such as ions, and RH, to clearly understand the self-assembly mechanism of the HTD-*n*–Pt's.

Platinum Ion Effect. The self-assembled morphologies of the HTD-*n* (0.05 g)/DMF (18.5 mL) and HTD-*n*–Pt (0.05 g)/DMF (18.5 mL) obtained at 288 K and 20% RH are shown in Figure 4. HTD-*n* can self-assemble into irregular silklike patterns [Figure 4(a–d)]; this was attributed to the secondary aggregation of unimolecular micelles stabilized by intermolecular hydrogen bonding.[34] However, HTD-*n*–Pt self-assembled into ordered 2D treelike supramolecular structures [Figure 4(e–h)] with a diameter of about 100–300 μm, and the diameter increased first and then decreased with increasing molecular weight. HTD-1–Pt, with a lower molecular weight, formed smaller micelle particles and took much more time to self-assemble into treelike aggregates, similar to those from HTD-2–Pt and HTD-3–Pt. HTD-4–Pt, with a higher molecular weight, formed bigger micelle particles that moved only in a limited region. Therefore, the sizes of the self-assembled HTD-1–Pt (155.40 ± 27.53 μm) and HTD-4–Pt (109.44 ± 15.39 μm) were smaller than those from HTD-2–Pt (215.45 ± 43.84 μm) and HTD-3–Pt (160.24 ± 20.75 μm), as confirmed by the statistical results obtained from 100 treelike self-assemblies.

Concentration Effect. Figure 5 shows the effect of the HTD-2–Pt concentration on its self-assembled morphology. With increasing concentration from 0.10 to 0.75 wt %, the morphology changed from an ordered treelike structure with fractal properties [Figure 5(a) and Figure 4(f)] to random rodlike, branchlike, or quarter-tree-like structures [Figure 4(b,c)]. HTD-2–Pt with a concentration of 0.10 wt % generated small flowerlike or half-tree-like aggregates [Figure 5(a)] rather than an ordered treelike structure [Figure 4(f)]; this was probably due to the lack of micelle particles to aggregate further on the surface. Although the self-assembling HTD-2–Pt had a higher concentration, the movement of micelle particles toward primitive aggregates may have become difficult because there was not enough space for rearrangement, and this resulted in rodlike or quarter-tree-like morphologies [Figure 5(b,c)].

Temperature and RH. The movement of micelles and the vaporization speed of DMF on the surface of substrates were dependent on the RH and temperature. Generally, a higher RH results in a lower vaporization of DMF, and a higher temperature is conducive to the movement of micelles. The

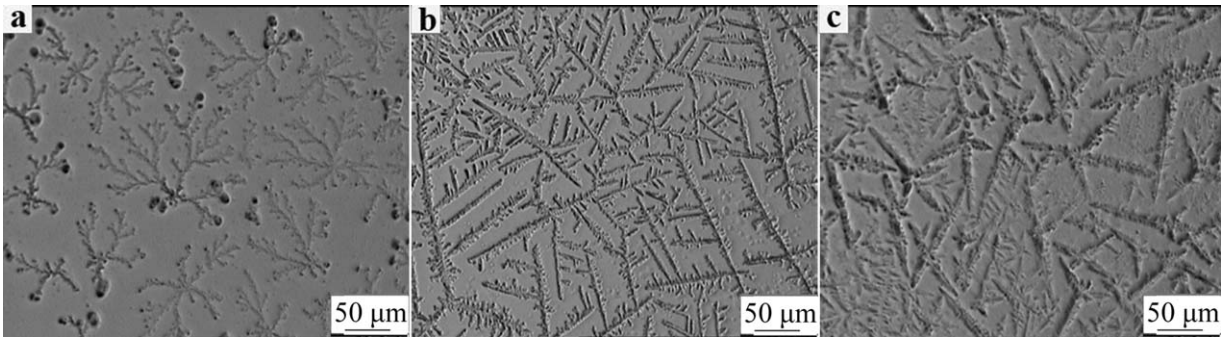

Figure 5. OM micrographs of the self-assembled HTD-2–Pt with different concentrations: (a) 0.10, (b) 0.40, and (c) 0.75 wt %.

morphologies of the self-assembled HTD-*n*–Pt with a 0.27 wt % concentration under different RHs and temperatures are shown in Figures 6 and 7, respectively. The micelle particles on the surface of the glass substrate aggregated together through the hydrogen bonding that they encountered at low RH, but the primitive aggregates could not rearrange, and this resulted in a partially regular treelike structure [Figure 6(a)]. On the contrary, the movement of micelle particles was too random to root in limited regions and form stable structures at high RH, so hazy wormlike [Figure 6(e)] and flecked aggregates [Figure 6(f,g)] were observed. With a medium RH of about 50%, these micelle particles were able to reassemble and form uniformly rulerlike structures [Figure 6(a–d)].

Low temperatures appeared to also be an indispensable factor for the formation of treelike self-assemblies [Figure 4(b)]. With increasing temperature, the morphologies (Figure 7) become irregular, consisting of cross-shaped patterns, and the size of the self-assemblies decreased sharply. The self-assembly temperature influenced not only the volatility rate of the DMF but also the movability of the micelle particles. With increasing temperature, the micelle particles may not have had enough time to rearrange into their preferred and stable morphology because of the fast vaporization of the solvent; this resulted in a smaller size and vague morphologies [Figure 7(e–h) cf. Figure 4(e–h)]. Polymers with higher molecular weights and bigger sizes also resulted in lower movability of the aggregated micelles. Therefore, only the micelle particles obtained from HTD-*n*–Pt with medium molecular weights could self-assemble into regular treelike [Figure 4(f,g)] and rulerlike structures [Figure 6(b,c)] with big sizes.

Self-Assembly Process and Mechanism. The previous results concerning the factors influencing self-assembly morphologies suggest that the platinum ions played a crucial role in inducing self-assembly. The coordination between platinum ions and carboxyl groups in HTD-*n* was confirmed by the FTIR and XPS spectra shown in Figure 2. The FTIR spectra of the self-assembled HTD-*n*–Pt's are shown in Figure 8(a). The absorption peak near 1610 cm^{-1} [Figure 2(a)] shifted to 1655 cm^{-1} [Figure 8(a)]; this indicated the formation of ordered treelike self-assemblies.

The XPS spectra of the self-assembled HTD-*n*–Pt's are shown in Figure 8(b–d). Peaks of BE at about 284.64 and 532.15 eV were attributed to C1s and O1s electrons, respectively, and the peaks around BEs of 72.52 and 75.87 eV were attributed to their $Pt_4f_{7/2}$ and $Pt_4f_{5/2}$ electrons. The decrease in BE of about

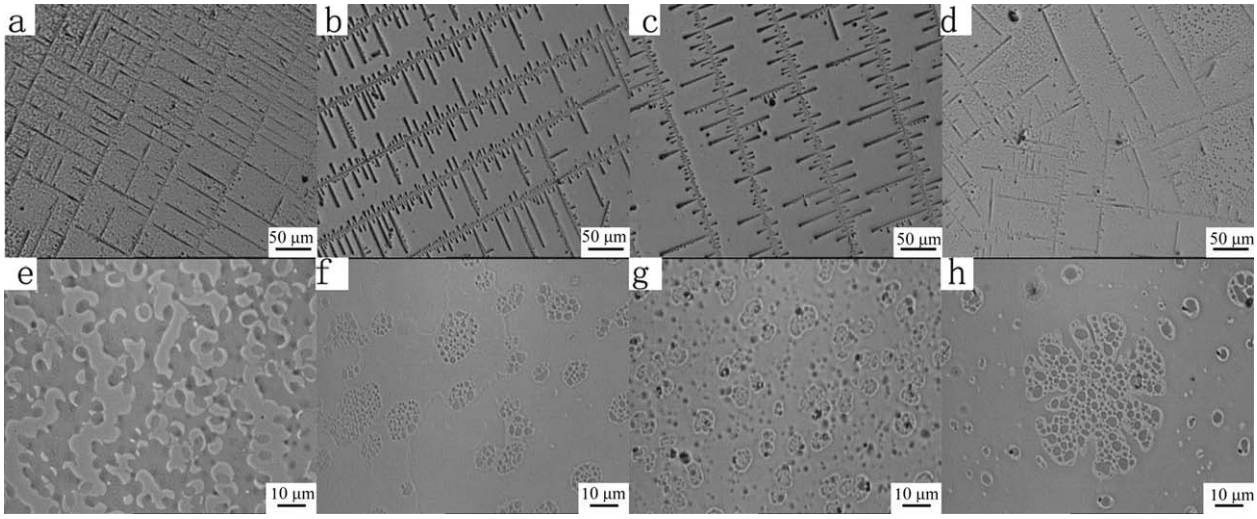

Figure 6. OM micrographs of the self-assembled HTD-*n*–Pt at various humidities: (a) HTD-1–Pt at 50% RH, (b) HTD-2–Pt at 50% RH, (c) HTD-3–Pt at 50% RH, (d) HTD-4–Pt at 50% RH, (e) HTD-1–Pt at 80% RH, (f) HTD-2–Pt at 80% RH, (g) HTD-3–Pt at 80% RH, and (h) HTD-4–Pt at 80% RH.

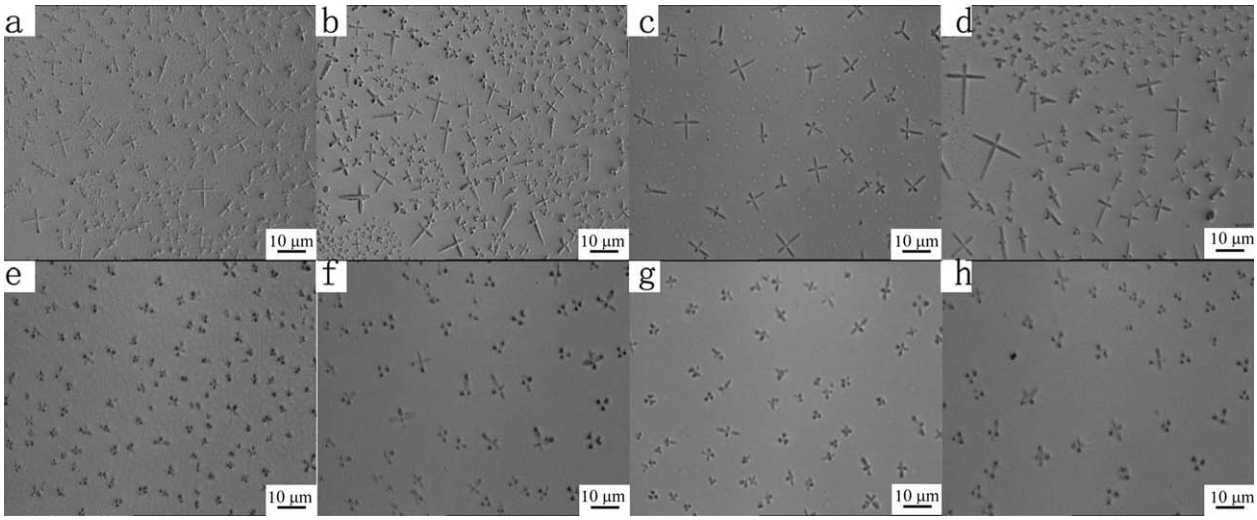

Figure 7. OM micrographs of the self-assembled HTD-*n*–Pt at various temperatures: (a) HTD-1–Pt at 313 K, (b) HTD-2–Pt at 313 K, (c) HTD-3–Pt at 313 K, (d) HTD-4–Pt at 313 K, (e) HTD-1–Pt at 353 K, (f) HTD-2–Pt at 353 K, (g) HTD-3–Pt at 353 K, and (h) HTD-4–Pt at 353 K.

0.5 eV for both the $Pt_4f_{7/2}$ and $Pt_4f_{5/2}$ electrons and the increase in BE of about 0.2 eV for the C1s electrons in the carboxyl groups also suggested the formation of ordered aggregates, as compared with the corresponding spectra shown in Figure 2. To analyze the effect of DMF during the self-assembly of the HTD-*n*–Pt's, both HTD-2 and HTD-2–Pt were dissolved in DMF, and the solutions were condensed to obtain solid samples. Compared with the XPS spectra of their self-assembled counterparts [Figure 8(d)], a distinct decrease in BE of the N1s electrons from about 401.40 to 400.64 and then to

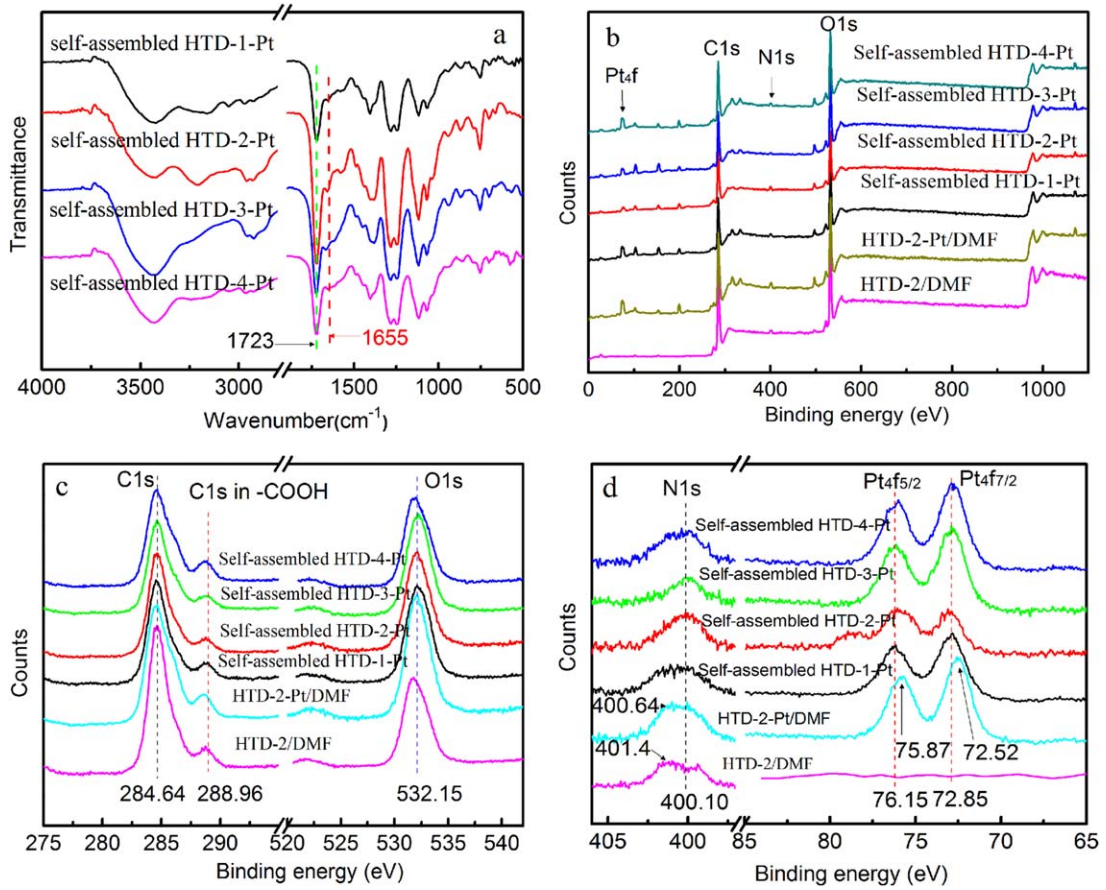

Figure 8. FTIR and XPS spectra of the self-assembled HTD-*n*–Pt and dried directly HTD-2/DMF and HTD-2–Pt/DMF. [Color figure can be viewed in the online issue, which is available at wileyonlinelibrary.com.]

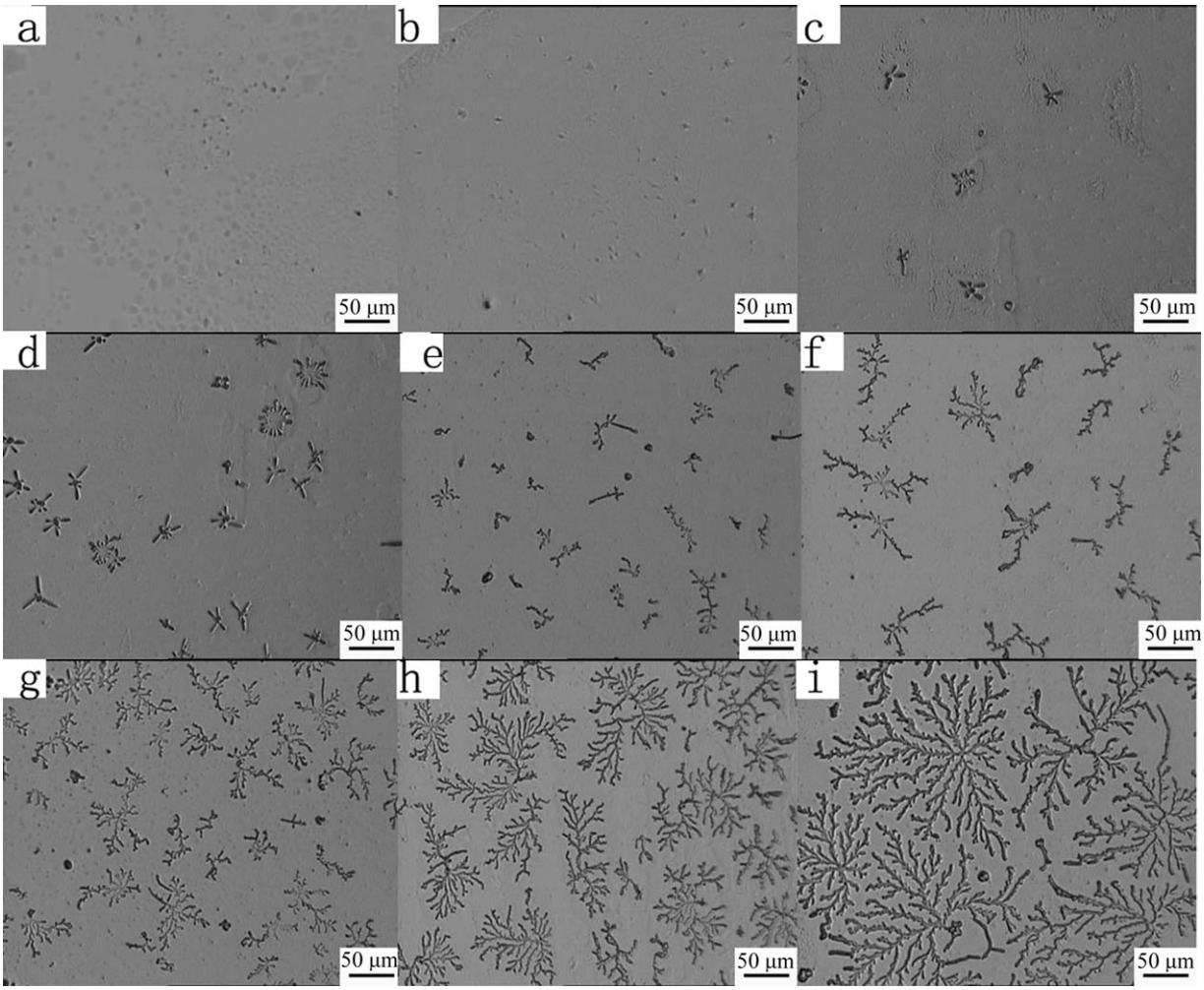

Figure 9. OM micrographs of the self-assembled HTD-2–Pt with 0.27 wt % concentration at 288 K and 20% RH: (a) 240, (b) 270, (c) 300, (d) 340, (e) 360, (f) 380, (g) 400, (h) 420, and (i) 460 min.

400.10 eV and an increase in BE of the $Pt4f_{7/2}$ and $Pt4f_{5/2}$ electrons from about 72.52 and 75.87 eV to 72.85 and 76.15 eV, respectively, clearly indicated a change in the interaction between the platinum and nitrogen atoms during self-assembly.

The surface self-assembly of HBPs or star polymers without metal ions usually results a in honeycomb structure, and the mechanism is supposed to be a combined solvent evaporation, water condensation, and core–shell micelle aggregation process.[35–38] The self-assembly mechanism of an HTD-3–Pt pyridine/ethyl acetate solution has been discussed according to one-dimensional microrodlike self-assemblies through water/oil micelles.[5] The selected solution could dissolve the core segments of HTD-3–Pt but not its peripheral segments composed of carboxyl and coordinate groups; this resulted in the formation of water/oil micelles. However, DMF can only dissolve the peripheral segments of HTD-*n*–Pt and form oil/water micelles; this resulted in perfect 2D ordered treelike supramolecular structures. Therefore, the mechanism of self-assembly through oil/water micelles was apparently different from that through water/oil micelles, although the solvent evaporation and concentration effects involved had similarity.[5,20] The effect of the self-assembly time on the morphology of the self-assembled HTD-2–Pt (Figure 9) suggested that the ordered treelike structures grew gradually and finally formed stable treelike structures with diameters of about 100–300 μm [Figure 9(i)] and a trunk width of about 2–3 μm (Figure 10). Moreover, the treelike morphology was very similar to those of conjugated polymers[39] and dendrimers,[40] and the process could be explained by the diffusion-limited aggregation (DLA) theory[41] of particles.

According to the self-assembly process of the HTD-2–Pt and DLA model, a possible self-assembly mechanism was proposed as follows:

1. The solubility parameter of the peripheral segments [mainly carboxyl groups; 22.22 $(J/cm^3)^{0.5}$] of HTD-*n*–Pt was close to that of DMF [24.80 $(J/cm^3)^{0.5}$], which existed as a distinct gap with that of the core chains of HTD-*n*–Pt [ca. 19.36–19.48 $(J/cm^3)^{0.5}$] without consideration of the coordinate and carboxyl groups. Thus, the complexes may have been amphiphilic polymers in DMF and could form micelles. When the HTD-*n*–Pt dispersed in DMF, the peripheral chains swelled and dissolved

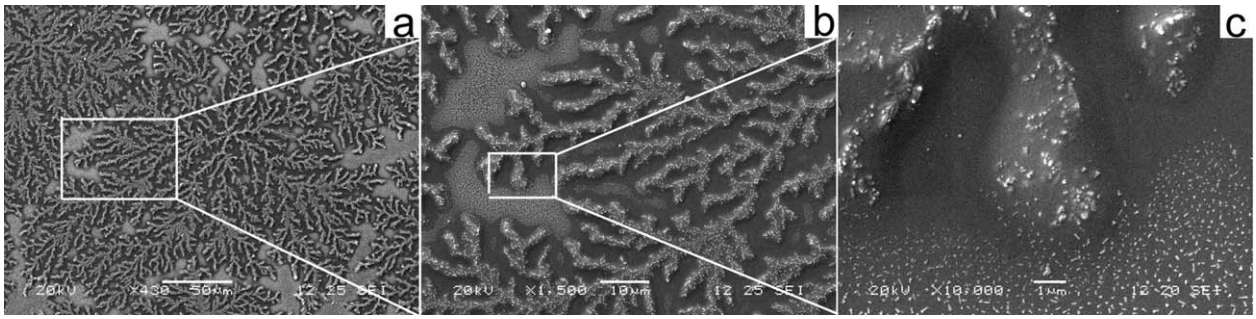

Figure 10. Scanning electron micrographs of the self-assembled HTD-2–Pt at various magnifications.

gradually, but the core chains shrank and deformed. This resulted in oil/water micelles (or primitive particles), substantiated by the D_h values of HTD-1–Pt, HTD-2–Pt, HTD-3–Pt, and HTD-4–Pt in DMF of about 83.7, 68.8, 195.1, and 129.2 nm, respectively (Figure 11). Moreover, the *p*s of HTD-*n*–Pt, as estimated in Table I, were in the range 0.5–1.0. This indicated that lamellar aggregates or vesicles were formed according to a previous study of the self-assembly of amphiphilic polymers.[13]

2. After the HTD-*n*–Pt solution, consisting of oil/water micelles, spread homogeneously on the substrate [Figure 9(a)], the micelles gradually formed separate aggregates [Figure 9(b)] with a diameter of about 300–500 nm [Figure 10(c)]. As the solvent evaporated, the decrease in the temperature of the aggregates may have resulted in the formation of water droplets on the surface of the aggregates,[36] and the aggregates thus shrink. The evaporation of DMF also drove the aggregates to move together and rearrange through hydrogen bonding and coordination interactions; this resulted in the formation of primitive self-assemblies [named *saplings,* Figure 9(c–e)]. With the further evaporation of DMF, some aggregates moved and met the saplings in a limited region. This resulted in the gradual growth [Figure 9(f–h)] of the saplings and, finally, the formation of mature trees [Figure 9(i)]. (3) The movement of the aggregates was similar to that of particles in the DLA model,[41] and the primitive self-assemblies and aggregates are regarded as seeds or single particles in DLA theory. A seed, as a core or sapling in the self-assembly system, was situated at the origin of a local region, and then a single particle (or aggregate) was near the original region. The particle moved randomly with the evaporation of DMF until it met a site adjacent to the seed. Then, the moving particle became a part of the primitive self-assembly. Another particle could then move randomly over until it joined the self-assembly [Figure 9(e–h)] and gradually formed a hyperbranched structure [Figure 9(i)]. This was demonstrated from the appearance of some separate aggregates with diameters of about 300–500 nm [Figure 10(c)]. The exposed ends of the self-assembly tended to grow more rapidly than other perimeter sites because the perimeter sites near the center were shadowed. Finally, treelike self-assemblies with excellent supramolecular structures formed, as shown in Figure 10(a).

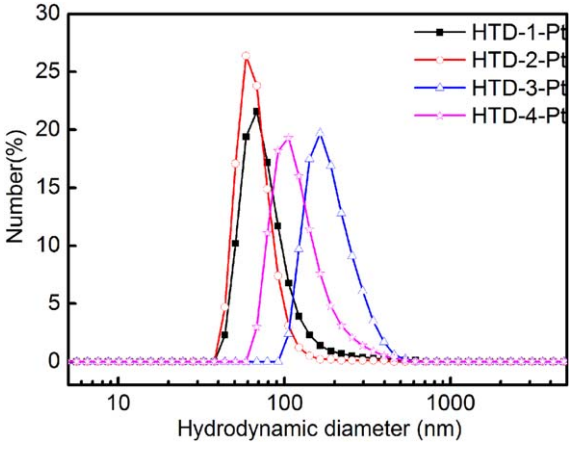

Figure 11. D_h values of HTD-*n*–Pt measured by DLS. [Color figure can be viewed in the online issue, which is available at wileyonlinelibrary.com.]

Properties of the Self-Assemblies. No sharp peaks appeared at low 2θs, as shown by the XRD spectra of the self-assembled HTD-*n*–Pt's in Figure 12(a); this suggested an amorphous structure of all of the self-assembled HTD-*n*–Pt's, and this agreed well with traditional self-assemblies obtained from amphiphilic HBPs.[11,18,42] Some weak peaks were attributed to the microcrystal structure fabricated by platinum ion coordination and hydrogen bonds during solvent-driven self-assembly.[5,19] The treelike structures were fabricated by single particles composed of the peripheral aggregation of primitive particles (Figure 10), and the core chains of particles could not rearrange because the condensed water droplets only swelled the peripheral hydrophilic chains. Therefore, the molecular chains of HTD-*n*–Pt still retained their intrinsic amorphous structure.

The resulting fractal behavior of the treelike self-assemblies in Figure 4 was very similar to that of self-assemblies from block polymers[43,44] and dendrimers.[45] The dimensions of fractal micrographs are usual between 1 and 2 for many clusters and aggregates according to DLA theory.[46] Generally, the higher the dimension is, the more orderly the structure becomes. The fractal dimension (D_f) could be calculated by the following equation[47] via the DLA model:

$$D_f = \lim_{r \to 0} \frac{\log N(r)}{\log (r)}$$

where r is the length unit and $N(r)$ is the size of the geometric object measured with the unit r. The relationships between

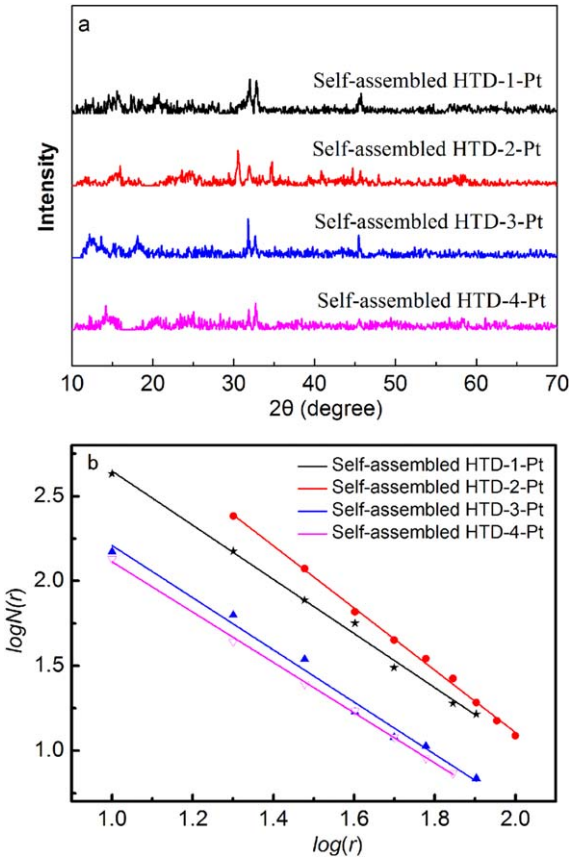

Figure 12. (a) XRD spectra of HTD-*n*–Pt, HTD-2 and self-assembled HTD-*n*–Pt and (b) D_f's of self-assembled HTD-*n*–Pt. [Color figure can be viewed in the online issue, which is available at wileyonlinelibrary.com.]

log $N(r)$ and log r in self-assembled HTD-*n*–Pt are shown in Figure 12(b), and the D_fs of HTD-1–Pt, HTD-2–Pt, HTD-3–Pt, and HTD-4–Pt self-assemblies were about 1.59, 1.83, 1.54, and 1.48, respectively. This indicated that the D_f of the self-assembled HTD-*n*–Pt's increased first and then decreased with increases in their molecular weight; this was in good agreement with their sizes of self-assemblies shown in Figure 4. This result could be explained by their self-assembly processes and influencing factors. The morphology of the self-assembled HTD-2–Pt was indeed more regular than those of the other three complexes.

CONCLUSIONS

On the basis of our previous studies of the solvent-driven self-assembly of both HTD-3–Pt and HTD-2–Pt with higher catalytic properties for hydrosilylation than traditional homogeneous catalysts, here we have reported their surface self-assembly in addition to that of HTD-1–Pt and HTD-4–Pt. Factors influencing the morphology of the self-assemblies, including the molecular weight, temperature, time, concentration, and RH, have also been discussed, and the 2D ordered treelike supramolecular structure on a micrometer scale was fabricated on the surface of a glass substrate. A self-assembly mechanism, in accordance with DLA theory, has been suggested. We highlighted the effect of the molecular weight of the hyperbranched polyesters on the catalytic activity and morphology control of self-assembly, and the results indicate that both HTD-2–Pt and HTD-3–Pt, with medium molecular weights, had better catalytic performance for hydrosilylation and self-assembled into more orderly and bigger microstructures than the other two complexes, with lower or higher molecular weights. All of the D_f's of the treelike self-assemblies increased first and then decreased with increasing molecular weight.

ACKNOWLEDGMENTS

The authors gratefully acknowledge the financial support of the National Natural Science Foundation of China (contract grant number 51373200), Program for New Century Excellent Talents in University (contract grant number NCET-13–1049), and Hubei Provincial Department of Education Science Research Program (contract grant number Q20131505).

REFERENCES

1. Troegel, D.; Stohrer, J. *Coord. Chem. Rev.* **2011**, *255*, 1440.
2. Downing, C. M.; Kung, H. H. *Catal. Commun.* **2011**, *12*, 1166.
3. Konkolewicz, D.; Monteiro, M. J.; Perrier, S. B. *Macromolecules* **2011**, *44*, 7067.
4. Voit, B. I.; Lederer, A. *Chem. Rev.* **2009**, *109*, 5924.
5. Zhang, D.; Wang, J.; Chen, S.; Cheng, X.; Li, T.; Zhang, J.; Zhang, A. *Langmuir* **2012**, *28*, 16772.
6. Zhou, Y.; Huang, W.; Liu, J.; Zhu, X.; Yan, D. *Adv. Mater.* **2010**, *22*, 4567.
7. Aida, T.; Meijer, E.; Stupp, S. *Science* **2012**, *335*, 813.
8. Jin, H.; Huang, W.; Zhu, X.; Zhou, Y.; Yan, D. *Chem. Soc. Rev.* **2012**, *41*, 5986.
9. Mann, S. *Nat. Mater.* **2009**, *8*, 781.
10. Dhar, J.; Patil, S. *ACS Appl. Mater. Interfaces* **2012**, *4*, 1803.
11. Peleshanko, S.; Tsukruk, V. V. *J. Polym. Sci. Part B: Polym. Phys.* **2012**, *50*, 83.
12. Chen, S.; Cheng, S. X.; Zhuo, R. X. *Macromol. Biosci.* **2011**, *11*, 576.
13. Mai, Y.; Eisenberg, A. *Chem. Soc. Rev.* **2012**, *41*, 5969.
14. Percec, V.; Wilson, D. A.; Leowanawat, P.; Wilson, C. J.; Hughes, A. D.; Kaucher, M. S.; Hammer, D. A.; Levine, D. H.; Kim, A. J.; Bates, F. S. *Science* **2010**, *328*, 1009.
15. Chen, C.; Liu, G.; Liu, X.; Pang, S.; Zhu, C.; Lv, L.; Ji, J. *Polym. Chem.* **2011**, *2*, 1389.
16. Wang, R.; Jiang, X.; Yu, B.; Yin, J. *Soft Matter* **2011**, *7*, 8619.
17. Tao, W.; Liu, Y.; Jiang, B.; Yu, S.; Huang, W.; Zhou, Y.; Yan, D. *J. Am. Chem. Soc.* **2012**, *134*, 762.
18. Zhou, Y.; Yan, D. *Chem. Commun.* **2009**, *10*, 1172.
19. Zhang, D.; Wang, J.; Chen, S.; Cheng, X.; Li, T.; Zhang, J.; Zhang, A. *Sci. Adv. Mater.* **2013**, *5*, 647.
20. Zhang, D.; Li, J.; Chen, S.; Li, T.; Zhou, J.; Cheng, X.; Zhang, A. *Macromol. Chem. Phys.* **2013**, *214*, 370.
21. Li, S.; Li, J.; Chen, S.; Zhang, D.; Li, T.; Zhang, J.; Chen, S.; Zhang, A. *Mater. Chem. Phys.* **2013**, *142*, 513.

22. Li, J.; Zhang, D.; Li, S.; Xu, Z.; Chen, S.; Li, T.; Zhang, J.; Chen, S.; Zhang, A. *Macromol. Chem. Phys.* **2013**, *214*, 1724.
23. Zhang, D.; Li, J.; Wang, J.; Chen, S.; Zhou, J.; Li, T.; Zhang, J.; Zhang, A.; Liu, C. *RSC Adv.* **2013**, *3*, 17073.
24. Haxton, K. J.; Burt, H. M. *Dalton Trans.* **2008**, 5872.
25. Kostiainen, M. A.; Hiekkataipale, P.; dela Torre, J. A.; Nolte, R. J. M.; Cornelissen, J. J. L. M. *J. Mater. Chem.* **2011**, *21*, 2112.
26. Zhang, D.; Jia, D. *Eur. Polym. J.* **2006**, *42*, 711.
27. Zhang, D.; Jia, D.; Chen, S. *Macromol. Chem. Phys.* **2009**, *210*, 1159.
28. Freeman, T.; Evans, S.; Ulman, A. *Thin Solid Films* **1994**, *244*, 784.
29. Freeman, T.; Evans, S.; Ulman, A. *Langmuir* **1995**, *11*, 4411.
30. Rivera, E. J.; Barbosa, C.; Torres, R.; Rivera, H.; Fachini, E. R.; Green, T. W.; Connick, W. B.; Colón, J. L. *Inorg. Chem.* **2012**, *51*, 2777.
31. Zhang, D.; Jia, D.; Chen, Y. *J. Macromol. Sci. Pure Appl. Chem.* **2010**, *47*, 957.
32. Zhang, L.; Eisenberg, A. *J. Am. Chem. Soc.* **1996**, *118*, 3168.
33. Zhang, L.; Eisenberg, A. *Polym. Adv. Technol.* **1998**, *9*, 677.
34. Dong, W.; Zhou, Y.; Yan, D.; Li, H.; Liu, Y. *Phys. Chem. Chem. Phys.* **2007**, *9*, 1255.
35. Maruyama, N.; Koito, T.; Nishida, J.; Sawadaishi, T.; Cieren, X.; Ijiro, K.; Karthaus, O.; Shimomura, M. *Thin Solid Films* **1998**, *327*, 854.
36. Srinivasarao, M.; Collings, D.; Philips, A.; Patel, S. *Science* **2001**, *292*, 79.
37. Widawski, G.; Rawiso, M.; François, B. *Nature* **1994**, *369*, 387.
38. Matsumoto, A.; Odani, T.; Chikada, M.; Sada, K.; Miyata, M. *J. Am. Chem. Soc.* **1992**, *121*, 11122.
39. Gan, H.; Li, Y.; Liu, H.; Wang, S.; Li, C.; Yuan, M.; Liu, X.; Wang, C.; Jiang, L.; Zhu, D. *Biomacromolecules* **2007**, *8*, 1723.
40. Das, I.; Goel, N.; Agrawal, N. R.; Gupta, S. K. *J. Phys. Chem. B* **2010**, *114*, 12888.
41. Witten, T. A., Jr; Sander, L. M. *Phys. Rev. Lett.* **1981**, *47*, 1400.
42. Leung, K. C.-F.; Lau, K.-N. *Polym. Chem.* **2010**, *1*, 988.
43. Gao, L.; Shi, L.; An, Y.; Zhang, W.; Shen, X.; Guo, S.; He, B. *Langmuir* **2004**, *20*, 4787.
44. Schor, M.; Bolhuis, P. G. *PCCP* **2011**, *13*, 10457.
45. Jasmine, M. J.; Prasad, E. *J. Phys. Chem. B* **2010**, *114*, 7735.
46. Witten, T. A.; Sander, L. M. *Phys. Rev. B* **1983**, *27*, 5686.
47. Lomander, A.; Hwang, W. M.; Zhang, S. G. *Nano Lett.* **2005**, *5*, 1255.